Optimized Bidirectional DC-DC Converter Adapted to High Voltage Gain and Wide ZVS Range

Yiliang Li, Yijie Wang, *Senior Member, IEEE*, Yueshi Guan, *Senior Member, IEEE*, and Dianguo Xu, *Fellow, IEEE*

***Abstract*—As a key component connecting dc microgrid and energy storage system, dual active bridge (DAB) converter has some inherent problems under high gain conditions. To solve the problems, this article proposes a half-bridge cascaded DAB converter with partial switch sharing. The converter combines the advantages of high voltage gain, wide soft switching range and less reactive backflow loss, under a hybrid modulation strategy based on pulsewidth modulation control and phase-shift control. In this article, the output power, soft switching characteristic and reactive backflow loss are analyzed in detail. By using the Karush–Kuhn–Tucker function method to achieve multiobjective optimization, the system can achieve the zero voltage switch (ZVS) turn-ON and reduce the reactive backflow loss. Moreover, the coupled relationships among variables are clarified clearly, and the system can achieve high voltage gain at low turns ratio. A 500 W, 100 kHz experimental prototype is built to verify the correctness of the theoretical analysis.**

***Index Terms*—Bidirectional dc/dc (BDC) converter, phase shift control, soft-switching, switch sharing.**

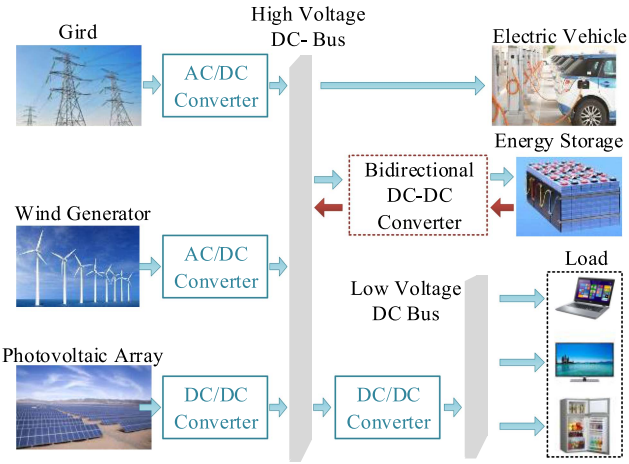

Fig. 1. DC microgrids system structure based on distributed generation.

I. Introduction

As THE penetration rate of renewable energy increases, the stable operation and power quality of microgrid are facing new challenges [1], [2]. Energy storage system has attracted extensive attention as an effective way to ensure the safe operation and efficiency improvement of microgrid [3], [4]. Fig. 1 shows the structure of the dc microgrids system based on distributed generation. The high-performance bidirectional dc/dc (BDC) converter, which connects the microgrid and the energy storage system, is an essential interface circuit to control the bidirectional flow of energy, maintain the stability of the grid voltage, and improve the power quality of the dc grid [5], [6].

BDC converter can be divided into two categories: nonisolated and isolated and suitable for different application scenarios [7]. Compared with the nonisolated BDC, the isolated BDC has electrical isolation between the voltage of transformer on both sides. By connecting the dc bus with the energy storage system of different voltage levels through the isolation transformer, the reliability and stability of the microgrid system are improved. Therefore, isolated BDC converters are more suitable for energy storage systems with high safety requirements [8], [9], [10]. As a representative circuit in isolated BDC, dual active bridge (DAB) converter has become a research hotspot due to its advantages of symmetrical circuit structure, good soft-switching characteristics and large transmission power capacity [11], [12]. The DAB converter relies on the voltage difference between the two ends of the inductor to achieve power transmission. Therefore, single phase shift (SPS) control is the common control method of the DAB converter which is simple and easy to implement [13], [14].

In microgrid applications with high voltage gain, DAB converter with SPS control has some fundamental issues, for instance, high reactive backflow loss and poor soft switching characteristics [15]. To address these issue, different methods are proposed, such as hardware optimization and software optimization. To improve the voltage and power level of BDC, device series-parallel is the most typical technical idea. However, the consistency of switches brings great risks to device series technology [16], [17]. On the basis of the device series-parallel scheme, Zhao et al. [18] and Liserre et al. [19], respectively, propose the structure based on a modular multilevel BDC, which enhances the reliability of the system. But each sub-module cannot work independently, reducing the control flexibility of the system. Tan et al. [20] and Wu et al. [21] propose the cascade structure with two converters connected in series. By adjusting

Manuscript received 26 June 2022; revised 26 September 2022; accepted 9 November 2022. Date of publication 14 November 2022; date of current version 26 December 2022. This work was supported by the National Natural Science Foundation of China under Grant 52007041. Recommended for publication by Associate Editor G. Moschopoulos. *(Corresponding author: Yijie Wang.)*

The authors are with the School of Electrical Engineering and Automation, Harbin Institute of Technology, Harbin 150001, China (e-mail: liylhit@qq.com; wangyijie@hit.edu.cn; hitguanyueshi@163.com; xudiang@hit.edu.cn).

Color versions of one or more figures in this article are available at https://doi.org/10.1109/TPEL.2022.3221946.

Digital Object Identifier 10.1109/TPEL.2022.3221946

the front-stage pulsewidth modulation (PWM) converter or the buck/boost converter, the rear-stage DAB circuit can achieve voltage matching. While the step-down ability of the front circuit is limited, and the buck/boost capability of the system is still completed by the transformer of the post-stage DAB circuit. What's more, a partial parallel DAB converter, is proposed to achieve high gain and low current stress in article [22]. However, the circuit structure of parallel converter module is complex and the number of components is large. Each module needs to have good consistency, otherwise the system requires additional control schemes to address the circulation between modules.

What's more, passive components are added to DAB circuit to form resonant circuit, such as *LC, LLC*, and *CLLC* resonant tank, are discussed in article [23], [24], [25]. The symmetric *CLLC* resonant converter can achieve soft-switching in the full load range, and has been widely used. However, on the secondary side of the *CLLC* converter, the capacitor of is large and the inductor is small, so it is difficult to design parameters under high gain conditions. What's more the resonant converter has strict requirements on parasitic parameters in the circuit. The asymmetric parasitic parameters of primary and secondary sides will affect the operation state of the system.

In terms of control strategy, extended phase shift (EPS), double phase shift, and triple phase shift (TPS) are successively proposed to optimize the performance of DAB converter. The optimization objectives of DAB include soft switching range, reactive backflow loss and current stress, which mainly affects the efficiency of the system [26], [27], [28]. Tian et al. [29] propose an optimal control strategy based on complete differential algorithm, which can achieve zero reactive backflow loss. In [30], inductor current is minimized at the moment of switch turn-OFF and the system realizes both zero voltage switch (ZVS) and minimum reactive backflow loss. However, the mathematical modeling of such controls is complex. Tong et al. [31] introduces an accurate model to describe the analytic expressions of the DAB converter under TPS control. Under the condition of different power levels, the reference proposes the global optimal condition equation, and the system achieves the minimum RMS current operation in the whole operating range. Similarly, Mahdavifard et al. [32] propose a hybrid control strategy based on asymmetric phase-shift control + TPS control, which can optimize the soft-switching and RMS current. However, the control system needs to determine the optimization interval in advance, which increases the amount of calculation. In addition, parameters optimization methods such as artificial intelligence algorithm and particle swarm optimization algorithm are applied in the design of DAB converter [33], [34].

With the rapid development of dc-power transmission, distribution and consumption systems, the interconnection and energy transmission between dc microgrid and energy storage system become urgent. Due to variable characteristics of storage system charging state, and low voltage-high power capacity battery technology, BDC converters are required to operate in high voltage gain. In order to obtain high gain under the condition of low transformer turns ratio, this article designs a half-bridge cascade DAB converter based partial switch sharing [35]. The article is organized as follow. In Section II, the circuit topology and operational principles are analyzed in detail. Section III derives transmission power characteristics, and optimizes the reactive backflow loss of the system. According to the control strategy, the soft-switching characteristics is analyzed in detail. In Section IV, the circuit parameters are optimized and an experimental prototype is built and tested to verify the validity of the theoretical analysis. Finally, the conclusion is drawn in Section V.

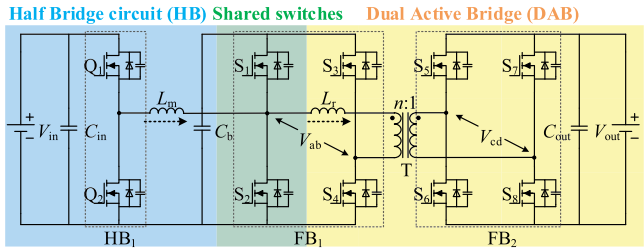

Fig. 2. Circuit topology of HB-DAB converter.

II. Circuit and Operation

Fig. 2 shows the circuit topology of the proposed HB-DAB converter. On the basis of the DAB circuit, it adds the voltage regulating half bridge HB_1 and the inductor L_m. Through the sharing of partial switches S_1 and S_2, the HB-DAB converter can reduce conduction loss and the number of switches, which can be considered as a one-and-half structure.

The HB-DAB converter adopts a hybrid control method. The half bridge HB_1 adopts PWM control, changing the duty cycle D_1 of switches Q_1 and Q_2, to adjust the bus voltage on the capacitor C_b. The DAB circuit adopts single-phase-shift control, and adjusts the phase shift d_D between full bridges FB_1 and FB_2 to control the magnitude and direction of energy transmission. In addition, a phase shift d_F is added between half-bridge HB_1 and full-bridge FB_1 to optimize the soft switching range of the shared switches. The switches on the same branch are complementary turn-ON with the same switching frequency.

When the converter operates in step-down mode, take the forward buck mode as an example to analyze the operation process of the proposed converter. To simplify the analysis, the following assumptions are made:

1) The energy storage components have no energy loss during discharging and charging progress.
2) The voltage fluctuation on the bus capacitor C_b is ignored and approximates to an ideal dc voltage source.
3) The dead time t_d is ignored, and the duty cycle of switches S_1-S_8 in DAB circuit is considered to be 0.5.
4) The switches are regarded as ideal active power devices, the resonance process in the dead time is ignored.

The turn-ON time of switch S_1 is taken as the reference zero phase. The phase is positive when the switch lags behind S_1 turn-ON. Conversely, the phase is negative. According to the relationship between the phase shift d_F, d_D and the duty cycle D_1, the proposed HB-DAB converter can be divided into four different operation conditions. Fig. 3 shows the driving signals of switches and the key steady-state waveforms in the circuit under

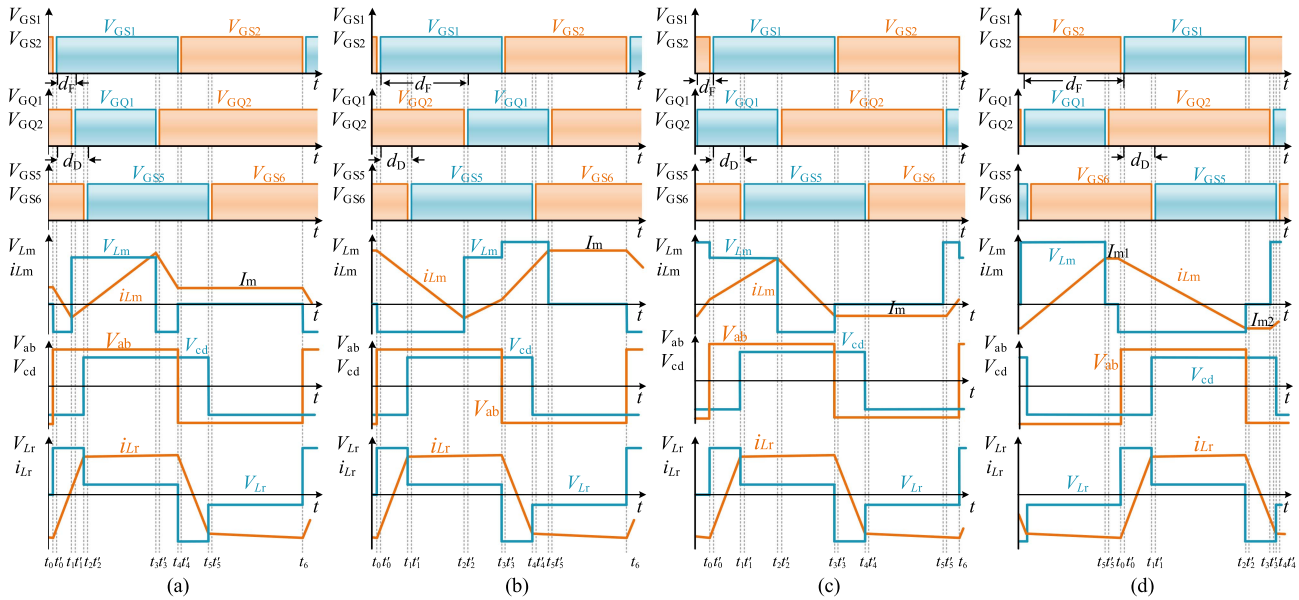

Fig. 3. Key waveforms of HB-DAB converter under different control strategies. (a) Control strategy I, $0<d_F<1\text{-}2D_1$. (b) Control strategy II, $1\text{-}2D_1<d_F<0.5$. (c) Control strategy III, $-2D_1<d_F<0$. (d) Control strategy IV, $-0.5<d_F<-2D_1$.

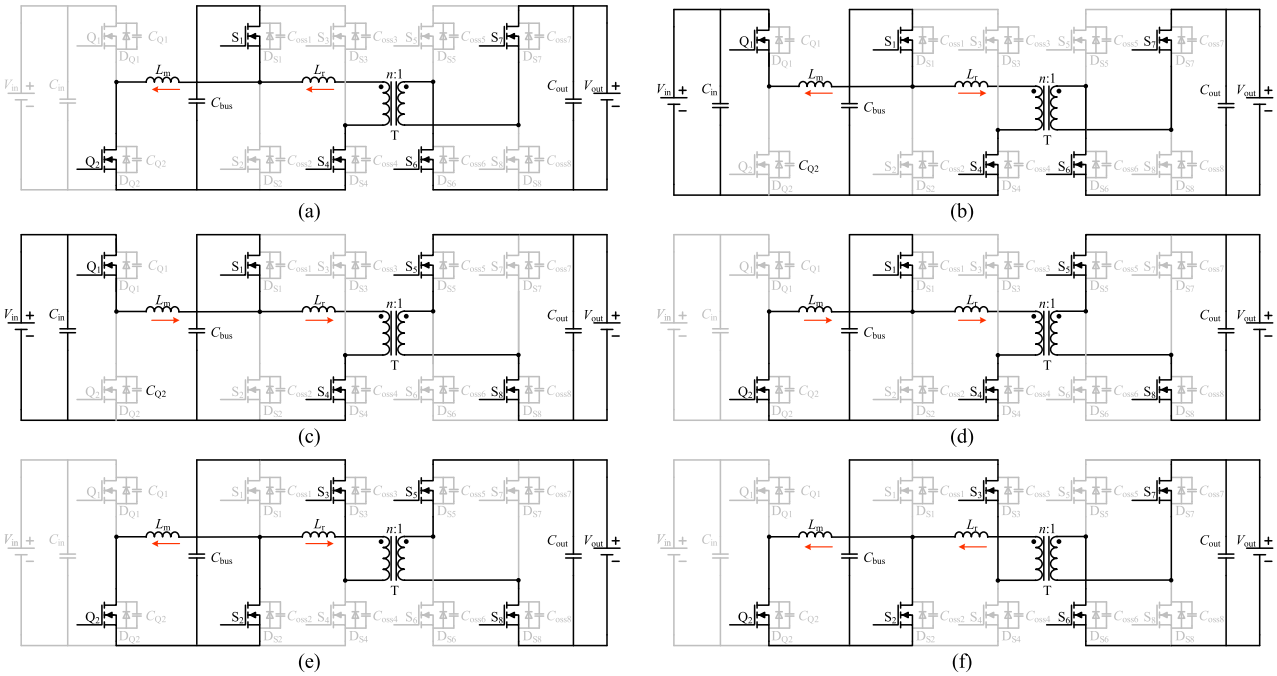

Fig. 4. Equivalent circuit diagram of the buck mode under the control strategy I. (a) Mode 1 [t_0, t_1]. (b) Mode 2 [t_1, t_2]. (c) Mode 3 [t_2, t_3]. (d) Mode 4 [t_3, t_4]. (e) Mode 5 [t_4, t_5]. (f) Mode 6 [t_5, t_6].

different operation conditions. The characteristics of the four control methods will be compared and analyzed in Section III. In this article, the first control method is selected which has smaller reactive backflow loss and good soft switching characteristics.

Take the turn-OFF time t_0 of switch S_2 as the starting point of the circuit operation analysis. The steady-state operation can be divided into six modes and the equivalent circuits are shown in Fig. 4.

1) *Mode* 1 [t_0, t_1]*:* At time t_0, S_2 and S_3 are turned-OFF and the full-bridge FB_1 enters the dead time. The inductor current i_{Lm} maintains the circulating current I_m of the *mode* 6. The reverse inductor current i_{Lr} discharges the parasitic capacitor of the switches and the body diodes D_{S1} and D_{S4} are turned ON. The voltage across switches S_1 and S_4 is clamped to zero. At time t'_0, switches S_1 and S_4 realize ZVS turn-ON. The inductor L_m transfer energy to keep the bus voltage V_b stable and supplies

power to the output terminal. At time t_1, switch Q_2 turns OFF and the half bridge HB_1 enters the dead time.

In this mode, the current flowing through the energy storage inductor L_m is calculated as

$$i_{Lm}(t) = I_m - \frac{V_b}{L_m}(t - t_0). \tag{1}$$

At time t_1, the inductor current $i_{Lm}(t_1)$ is calculated as

$$i_{Lm}(t_1) = I_m - \frac{V_b}{2L_m f} d_F \tag{2}$$

where $d_F = \varphi_F/180°$, φ_F is the phase difference between switches S_1 and Q_1 and V_b represents the voltage across the capacitor C_b.

2) *Mode* 2 [t_1, t_2]*:* At time t_1, the switch Q_2 turns OFF, and the half bridge HB_1 enters the dead time. The reverse inductor current i_{Lm} completes the charge and discharge of the parasitic capacitor of switches Q_1 and Q_2. At time t'_1, switch Q_1 realizes ZVS turn-ON. The input voltage V_{in} and the energy storage inductor L_m maintain the stability of the intermediate bus voltage V_b.

The current flowing through inductor L_r is calculated as

$$i_{Lr}(t) = i_{Lr}(t_0) + \frac{V_b + nV_{\text{out}}}{L_r}(t - t_0). \tag{3}$$

At time t_2, the inductor current $i_{Lr}(t_2)$ is calculated as

$$i_{Lr}(t_2) = i_{Lr}(t_0) + \frac{V_b + nV_{\text{out}}}{2L_r f} d_D \tag{4}$$

where n is the turns ratio of the transformer, d_D is calculated as $d_D = \varphi_D/180°$ and φ_D is the phase difference between S_1 and S_5.

3) *Mode* 3 [t_2, t_3]*:* At time t_2, switches S_6 and S_7 turn OFF. The forward inductor current i_{Lr} flows through the body diodes of the switch S_5 and S_8 after discharging the parasitic capacitor, which can realize the ZVS turn-ON.

In this mode, the inductor current i_{Lm} is calculated as

$$i_{Lm}(t) = i_{Lm}(t_1) + \frac{V_{\text{in}} - V_b}{L_m}(t - t_1). \tag{5}$$

At time t_3, the inductor current $i_{Lm}(t_3)$ is calculated as

$$i_{Lm}(t_3) = I_m - \frac{V_b}{2L_m f} d_F + \frac{V_{\text{in}} - V_b}{L_m f} D_1. \tag{6}$$

4) Mode 4 [t_3, t_4]*:* At time t_3, switch Q_1 turns OFF. The positive inductor current i_{Lm} clamps the voltage across switch Q_2 to zero. At time t'_3, switch Q_2 realizes ZVS turn-ON and input current $i_{in}(t)$ drops to zero. Inductor L_m freewheels through the loop formed by switches S_1 and Q_2, and keeps the bus voltage V_b stable.

The inductor current i_{Lm} is calculated as

$$i_{Lm}(t) = i_{Lm}(t_3) - \frac{V_b}{L_m}(t_4 - t_3). \tag{7}$$

At time t_4, the inductor current $i_{Lm}(t_4)$ is calculated as

$$i_{Lm}(t_4) = I_m + \frac{V_{\text{in}} D_1}{L_{\text{m}} f} - \frac{V_b}{2L_m f} = I_m. \tag{8}$$

In the mode 3 and mode 4, the current flowing through the leakage inductor L_r is calculated as

$$i_{Lr}(t) = i_{Lr}(t_2) + \frac{V_b - nV_{\text{out}}}{L_r}(t - t_2). \tag{9}$$

At time t_4, the inductor current $i_{Lr}(t_4)$ is calculated as

$$i_{Lr}(t_4) = i_{Lr}(t_0) + \frac{V_b - nV_{\text{out}}(1 - 2d_D)}{2L_r f}. \tag{10}$$

5) *Mode* 5 [t_4, t_5]*:* At time t_3, switches S_1 and S_4 turn OFF. The current i_{Lm} and i_{Lr} simultaneously charge and discharge the parasitic capacitor of switches S_2 and S_3. After switches S_2 and S_3 realizing ZVS turn ON, the voltage across the inductor L_m is zero and the inductor current i_{Lm} maintains at circulating current I_m, circulating through Q_2 and S_2.

In this mode, the inductor current i_{Lr} is calculated as

$$i_{Lr}(t) = i_{Lr}(t_4) - \frac{V_b + nV_{\text{out}}}{L_r}(t - t_4). \tag{11}$$

At time t_5, the inductor current $i_{Lr}(t_5)$ is calculated as

$$i_{Lr}(t_5) = i_{Lr}(t_0) + \frac{V_b - nV_{\text{out}}}{2L_r f}(1 - d_D). \tag{12}$$

6) *Mode* 6 [t_5, t_6]*:* At time t_5, the full bridge FB_2 enters dead time. At time t'_5, the reverse inductor current enables switches S_6 and S_7 to realize ZVS turn-ON. Inductor L_m maintains a circulating current state. The capacitor C_b transmits energy to the output side through S_6 and S_7.

In this mode, the inductor current i_{Lr} is calculated as

$$i_{Lr}(t) = i_{Lr}(t_5) + \frac{-V_b + nV_{\text{out}}}{L_r}(t - t_5). \tag{13}$$

At time t_6, the current flowing through the inductor L_r is calculated as

$$i_{Lr}(t_6) = i_{Lr}(t_0). \tag{14}$$

After the end of *mode* 6, the converter returns to *mode* 1 and periodically starts next operation cycle.

III. Research on Topology Characteristics

A. Output Characteristics Analysis

According to the analysis in Section II, the HB-DAB converter can be regarded as a combination of a constant voltage source and a constant power source. As the key device connecting the front and rear stages, capacitor C_b charges and discharges continuously in an operation cycle to maintain the stability of the output voltage V_{out}. To simplify the analysis, the charge-discharge loss of capacitor C_b is ignored, and the intermediate voltage V_b is assumed to remain constant in one operating cycle. According to formula (8), the voltage gain of the half bridge circuit can be calculated as follows:

$$V_b/V_{\text{in}} = 2D_1. \tag{15}$$

It can be concluded that when the input voltage V_{in} is constant, the voltage V_b is only related to the duty cycle D_1.

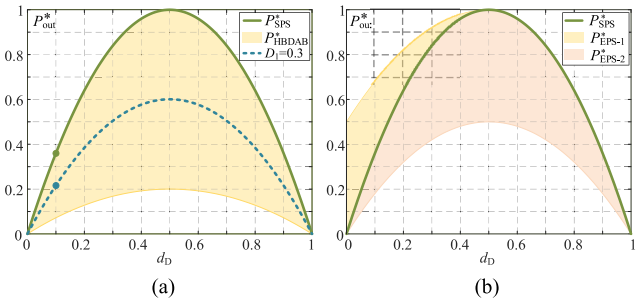

Fig. 5. Comparison of output power between HB-DAB and DAB converter. (a) Half-bridge cascaded DAB. (b) DAB under SPS, EPS control.

According to formula (9)–(14), integrating inductor current i_{Lr} in each mode, the output power can be calculated as

$$P_{\text{out}} = \frac{2}{T}\int_0^{t_3} V_{\text{b}} i_{Lr}(t)dt = \frac{nV_{\text{in}}V_{\text{out}}D_1}{L_r f} d_D(1-d_D). \quad (16)$$

The output power of the HB-DAB converter is similar to the traditional DAB converter, and both formulas are the same when $D_1 = 0.5$. Fig. 5 shows the comparison of the normalized transmission power P^*_{out} between the proposed converter and the DAB converter which is calculated as $P^*_{\text{out}} = P_{\text{out}}/P_{\max}$

$$P_{\max} = P_{\text{out}}|_{d_D=0.5} = \frac{nV_{\text{in}}V_{\text{out}}D_1}{4L_r f}. \quad (17)$$

Both EPS control strategy and the HB-DAB converter can change the output power of the system from a single curve to an adjustable region. By adjusting the duty cycle D_1 of the front half-bridge HB_1, the proposed converter has a wider power regulation range with a simpler and less computational control strategy, which can enhance the control flexibility.

It should be pointed out that the traditional DAB converter power distribution is not uniform. This shows that the power distribution of the DAB converter is dense under light load conditions. The effect of dead time cannot be ignored and a small change of the phase shift angle will lead to a large error in the output power. In contrast, as shown in Fig. 5(b), the output power of the HB-DAB converter can be approximately linearized under light load condition by adjusting duty cycle D_1. The transmission power error can be significantly reduced. Therefore, the converter shows better robustness under light load condition.

B. Soft Switching Characteristic Analysis

Soft-switching characteristic is an important indicator to determine the efficiency and reliability between dc microrad and energy storage system, especially in high frequency condition. The duty cycle D_1 of switch Q_1 is adjusted to achieve voltage matching of DAB circuit and an extra phase shift d_F is added between switches Q_1 and S_1 to expand the soft switching range of sharing switches.

Before the driving signal arrives, the reverse inductor current i_{Lm} and i_{Lr} need to flow through the body diode of the switches, and clamp the voltage across the switches to zero. To analyze the soft switching conditions of each switch, the directional relationship of inductor current i_{Lm} and i_{Lr} can be calculated as follows:

$$\begin{cases} Q_1 : i_{Q_1}(t_1) = i_{Lm}(t_1) < 0 \\ Q_2 : i_{Q_2}(t_3) = i_{Lm}(t_3) > 0 \\ S_1 : i_{S_1}(t_0) = i_{Lr}(t_0) - i_{Lm}(t_0) < 0 \\ S_2 : i_{S_2}(t_4) = i_{Lr}(t_4) - i_{Lm}(t_4) > 0 \\ S_3 : i_{S_3}(t_4) = i_{Lr}(t_4) > 0 \\ S_4 : i_{S_4}(t_0) = i_{Lr}(t_0) < 0 \\ S_{5/8} : i_{S_5}(t_2) = i_{S_8}(t_2) = i_{Lr}(t_2) > 0 \\ S_{6/7} : i_{S_6}(t_5) = i_{S_7}(t_5) = i_{Lr}(t_5) < 0 \end{cases}. \quad (18)$$

Ignoring the ESR loss on the capacitor C_b, the active power transmitted by the inductor L_m is equal to the active power at the output of the converter in one operation cycle. The circulating current I_m of the inductor current i_{Lm} in *modes* 5 and 6 is calculated as:

$$I_{\text{out}} = \frac{1}{T}\int_{t_0}^{t_4} i_{Lm}(t)dt$$

$$I_m = \frac{P_{\text{out}}}{V_{\text{in}}D_1} + \frac{V_{\text{in}}D_1(2D_1 + 2d_F - 1)}{2L_m f}. \quad (19)$$

Under steady-state conditions, the average current flowing through the inductor L_r is zero during one switching cycle, calculated as

$$i_{Lr}(t_0) = \frac{nV_{\text{out}} - 2D_1V_{\text{in}} - 2d_D nV_{\text{out}}}{4L_r f}. \quad (20)$$

According to the operation mode analysis of the system in Section II, the soft switching conditions of switches Q_1 and Q_2 can be deduced as follows:

$$\begin{cases} \frac{nV_{\text{out}}d_D(1-d_D)}{L_r f} - \frac{V_{\text{in}}D_1(1-2D_1)}{2L_m f} < 0 \\ \frac{nV_{\text{out}}d_D(1-d_D)}{L_r f} + \frac{V_{\text{in}}D_1(1-2D_1)}{2L_m f} > 0 \end{cases}. \quad (21)$$

The soft switching range of switches Q_1 and Q_2 is shown in Fig. 6. The gray plane corresponds to the ZVS plane. Switch Q_1 achieves soft switching where the part of the surface below ZVS plane. As shown in Fig. 6(a)–(c), the soft-switching range of switch Q_1 varies sinusoidally with duty cycle D_1 and phase shift d_D. With the increase of d_D, the soft switch range of Q_1 gradually decreases. In a certain voltage regulation range, the switch Q_1 has a wide soft switching range, especially the duty cycle is in the range of 0.1–0.4. Correspondingly, switch Q_2 can always realize the soft switching as the surface above the ZVS plane, which is consistent with the previous theoretical analysis.

The soft switching conditions of the switches S_3-S_8 can be calculated as:

$$\begin{cases} \frac{nV_{\text{out}}(1-2d_D)}{4L_r f} - \frac{V_{\text{in}}D_1}{2L_r f} < 0 \\ \frac{V_{\text{in}}D_1(2d_D-1)}{L_r f} + \frac{nV_{\text{out}}}{2L_r f} > 0 \end{cases}. \quad (22)$$

Fig. 7 compares the soft-switching range of switches $S_{3\text{-}8}$ between HB-DAB converter and DAB converter. Where K is the system gain, calculated as $V_{\text{in}}/nV_{\text{out}}$, representing the buck-boost capability of the system.

The shaded areas 1–4 in Fig. 7(a) correspond to the expanded soft-switching range under different duty cycles D_1 respectively. As shown by the shaded area in Fig. 7(b), the soft switching

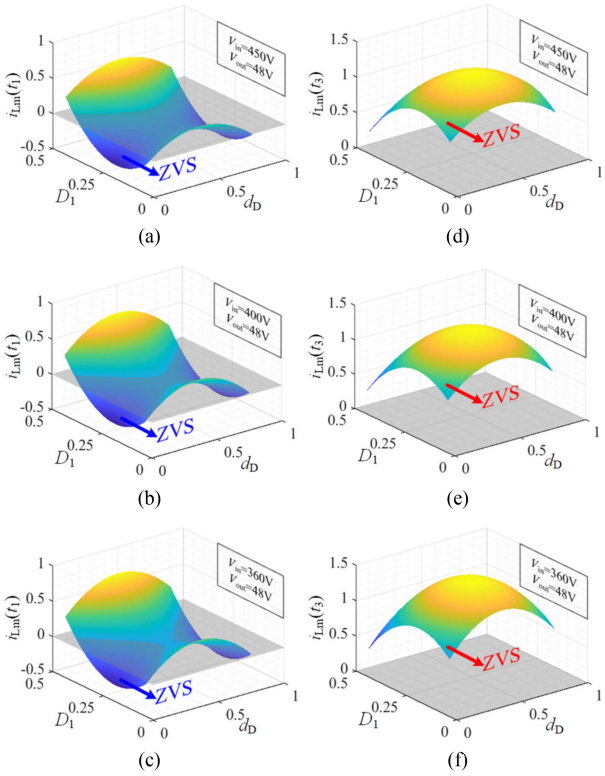

Fig. 6. Soft switching range of switches Q_1 and Q_2 under different conditions. (a) Q_1 ($V_{\text{in}} = 450$ V and $V_{\text{out}} = 48$ V). (b) Q_1 ($V_{\text{in}} = 400$ V and $V_{\text{out}} = 48$ V). (c) Q_1 ($V_{\text{in}} = 360$ V and $V_{\text{out}} = 48$ V). (d) Q_2 ($V_{\text{in}} = 450$ V and $V_{\text{out}} = 48$ V). (e) Q_2 ($V_{\text{in}} = 400$ V and $V_{\text{out}} = 48$ V). (f) Q_2 ($V_{\text{in}} = 360$ V and $V_{\text{out}} = 48$ V).

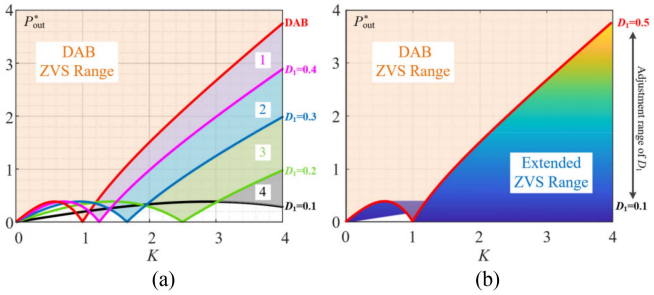

Fig. 7. Soft switching range of switches $S_{3\text{-}8}$. under different conditions. (a) Traditional DAB converter. (b) HB-DAB converter.

range of HB-DAB converter is significantly increased, which covers most of the hard-switching area of the traditional DAB converter. By adjusting the duty cycle D_1, the voltage stress across the inductor L_r can be optimized, under the high voltage gain and light load conditions.

As sharing switches, the soft switching of S_1 and S_2 are realized by the combined action of inductor currents $i_{Lm}(t)$ and $i_{Lr}(t)$. By designing the inductor current i_{Lr}, the ZVS turn-ON of S_1 and S_2 can be easily realized.

According to formula (10), the soft switching conditions of S_1 and S_2 can be calculated as

$$\begin{cases} i_{S_1}(t_0) = i_{Lr}(t_0) - i_{Lm}(t_0) < 0 \\ i_{S_2}(t_4) = i_{Lr}(t_4) - i_{Lm}(t_4) > 0 \end{cases}. \tag{23}$$

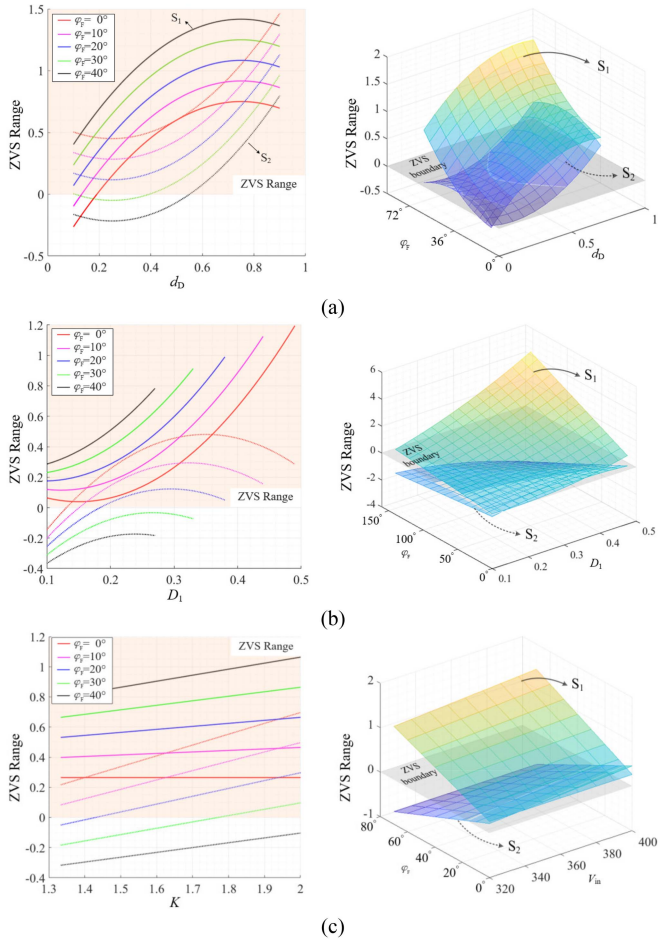

Fig. 8. Soft switching range of shared switches S_1 and S_2 under different conditions. (a) Influence of d_F and d_D. (b) Influence of d_F and D_1. (c) Influence of d_F and K.

Simplify as

$$i_{Lr}(t_0) < I_m < -i_{Lr}(t_0). \tag{24}$$

Inductor current $i_{Lr}(t_0)$ less than zero is a necessary condition for switches S_1 and S_2 to realize soft switching, which can completely discharge the parasitic capacitors of switches S_1 and S_2. When the inductor current $i_{Lm}(t_0)$ is close to zero, switches S_1 and S_2 can always achieve ZVS turn-ON with good soft switching characteristics.

Substitute formula (12) and (13) into the inequality above

$$\begin{cases} \frac{(1-2d_D)-2D_1K}{4L_rf} - \frac{D_1K(2D_1+2d_F-1)}{2L_mf} < \frac{d_D(1-d_D)}{L_rf} \\ \frac{(2d_D-1)+2D_1K}{4L_rf} - \frac{D_1K(2D_1+2d_F-1)}{2L_mf} > \frac{d_D(1-d_D)}{L_rf} \end{cases}. \tag{25}$$

Fig. 8 shows the variation curve of the soft switching range under different conditions of S_1 and S_2. The soft switching range of switches S_1 and S_2 can be expressed as the part of surface above the ZVS plane. The solid line and dotted line correspond to the soft switching of S_1 and S_2, respectively.

It can be conculcated that the soft switching condition of S_1 and S_2 is related to the voltage gain K, the duty cycle D_1, the phase shift d_D and d_F. With the increase of d_D, D_1 and K, the

TABLE I
COMPARISON OF CIRCULATING CURRENT AND REACTIVE RETURN LOSS UNDER DIFFERENT CONTROL STRATEGIES

Control Strategy	Circulating current I_{m}	Reactive backflow loss P_{bf}
I	$I_{\mathrm{m}}=\frac{P_{\mathrm{out}}}{V_{\mathrm{in}}D_1}+\frac{V_{\mathrm{in}}D_1(2D_1+2d_{\mathrm{F}}-1)}{2L_{\mathrm{m}}f}$	$P_{\mathrm{bf}}=\frac{L_{\mathrm{m}}}{2(1-2D_1)f}\left[\frac{nV_{\mathrm{out}}d_{\mathrm{D}}(1-d_{\mathrm{D}})}{L_{\mathrm{r}}}+\frac{V_{\mathrm{in}}D_1(2D_1-1)}{2L_{\mathrm{m}}}\right]^2$
II	$I_{\mathrm{m}}=\frac{P_{\mathrm{out}}}{D_1\cdot V_{\mathrm{in}}}+\frac{\left[2D_1-(d_{\mathrm{F}}-1)^2\right]V_{\mathrm{in}}}{4fL_{\mathrm{m}}}$	$P_{\mathrm{bf-1}}=\frac{L_m}{2(1-2D_1)f}\left\{\frac{\left[(1-d_{\mathrm{F}})^2+2D_1(2d_{\mathrm{F}}-1)\right]V_{\mathrm{in}}}{4L_m}-\frac{(1-d_{\mathrm{D}})d_{\mathrm{D}}nV_{\mathrm{out}}}{L_r}\right\}^2$ $P_{\mathrm{bf-2}}=\frac{\left[-2D_1+(d_{\mathrm{F}}-1)^2\right]V_{\mathrm{in}}}{4}\cdot\left\{\frac{\left[-2D_1+(d_{\mathrm{F}}-1)^2\right]V_{\mathrm{in}}}{8L_m}-\frac{d_{\mathrm{D}}(1-d_{\mathrm{D}})nV_{\mathrm{out}}}{L_r}\right\}$ $+\frac{d_{\mathrm{D}}(1-d_{\mathrm{D}})nV_{\mathrm{out}}L_m}{2fL_r}\left\{\frac{V_{\mathrm{in}}\left[4D_1+(d_{\mathrm{F}}-1)^2\right]}{2L_m}+\frac{(1-d_{\mathrm{D}})d_{\mathrm{D}}nV_{\mathrm{oct}}}{L_r}\right\}$
III	$I_{\mathrm{m}}=\frac{P_{\mathrm{out}}}{V_{\mathrm{in}}\cdot D_1}+\frac{V_{\mathrm{in}}\left[4D_1^2-2D_1(2d_{\mathrm{F}}+1)+d_{\mathrm{F}}^2\right]}{4L_{\mathrm{m}}f}$	$P_{\mathrm{bf-1}}=\frac{L_{\mathrm{m}}}{2f}\left[\frac{V_{\mathrm{in}}\left(4D_1^2+d_{\mathrm{F}}^2-2D_1-4D_1d_{\mathrm{F}}\right)}{4L_{\mathrm{m}}}+\frac{nV_{\mathrm{out}}d_{\mathrm{D}}(1-d_{\mathrm{D}})}{L_{\mathrm{r}}}\right]^2$ $P_{\mathrm{bf-2}}=-\frac{(2D_1-d_{\mathrm{F}})(2D_1-d_{\mathrm{F}}-1)d_{\mathrm{F}}V_{in}^2}{8L_{\mathrm{m}}f}-\frac{d_{\mathrm{D}}(1-d_{\mathrm{D}})d_{\mathrm{F}}V_{\mathrm{in}}nV_{\mathrm{out}}}{2L_{\mathrm{r}}f}$ $+\frac{L_{\mathrm{m}}}{2(1-2D_1)f}\left(\frac{(2D_1-d_{\mathrm{F}})(2D_1-d_{\mathrm{F}}-1)+d_{\mathrm{F}}}{4L_{\mathrm{m}}}V_{\mathrm{in}}+\frac{d_{\mathrm{D}}(1-d_{\mathrm{D}})nV_{\mathrm{out}}}{L_{\mathrm{r}}}\right)^2$
IV	$I_{\mathrm{m_1}}=\frac{P_{\mathrm{out}}}{D_1V_{\mathrm{in}}}+\frac{D_1V_{\mathrm{in}}}{2L_{\mathrm{m}}f}$ $I_{\mathrm{m_2}}=\frac{P_{\mathrm{out}}}{D_1\cdot V_{\mathrm{in}}}-\frac{D_1-V_{\mathrm{in}}}{2L_{\mathrm{m}}f}$	$P_{\mathrm{bf}}=\frac{L_{\mathrm{m}}}{2f}\left(\frac{D_1V_{\mathrm{in}}}{2L_{\mathrm{m}}}-\frac{(1-d_{\mathrm{D}})d_{\mathrm{D}}nV_{\mathrm{out}}}{L_{\mathrm{r}}}\right)^2$

soft switching range of switches S_1 and S_2 gradually increases. But according to Fig. 8(a)–(c), the effect of phase shift d_F on the soft switching of S_1 and S_2 shows an opposite trend. With the phase shift d_F increases, the soft-switching range of switch S_1 increases, but that of switch S_2 decreases.

To extend the soft switching range, the design of phase shift d_F is optimized. According to formula (6), (8), and (19), the maximum and minimum values of the inductor current i_{Lm} are calculated as follows:

$$i_{Lm-\max}=\frac{nV_{\mathrm{out}}d_D(1-d_D)}{fL_r}+\frac{V_{\mathrm{in}}D_1(1+2D_1)}{L_mf} \tag{26}$$

$$i_{Lm-\min}=\frac{nV_{\mathrm{out}}d_D(1-d_D)}{fL_r}-\frac{V_{\mathrm{in}}D_1(1-2D_1)}{2L_mf}. \tag{27}$$

It can be concluded that the current stress of the inductor L_m is independent of the phase shift d_F. By changing the phase shift d_F, the circulating current I_m is adjusted and the effective value of the inductor current i_{Lm} can be optimized.

When the circulating current I_m is close to zero, the RMS value of inductor current i_{Lm} is lower and switches S_1 and S_2 can realize ZVS turn-ON. The current I_m is approximately equal to zero, and calculate the phase shift d_F as follows:

$$d_F=\frac{1-2D_1}{2}-\frac{nV_{\mathrm{out}}d_D(1-d_D)L_m}{V_{\mathrm{in}}D_1L_r}. \tag{28}$$

C. Reactive Backflow Loss Analysis

According to the operation analysis in Section II, the reverse inductor current i_{Lm} is a necessary condition for the switch to realize ZVS turn-ON. But, the input voltages and currents of different phases inevitably causes reactive backflow loss in *mode* 2. Similarly, this is a fundamental issue in the traditional DAB converter, especially under full load conditions. The reactive backflow loss does not contribute to the output power, causes additional stress to the devices and reduces the efficiency of the system. In the dc microgrid system, the large reactive backflow loss will cause disturbance to the dc grid, reducing the stability and safety of the system.

According to formula (2), the input current $i_{\mathrm{in}}(t_1)$ is

$$i_{\mathrm{in}}(t_1)=\frac{nV_{\mathrm{out}}d_D(1-d_D)}{L_rf}+\frac{V_{\mathrm{in}}D_1(2D_1-1)}{2L_mf}. \tag{29}$$

According to formula (5), the duration of the reverse input current is calculated as

$$\Delta t=\frac{D_1}{2f}+\frac{d_D(1-d_D)nV_{\mathrm{out}}L_{\mathrm{m}}}{(2D_1-1)V_{\mathrm{in}}L_rf}. \tag{30}$$

Combining formulas (29) and (30), the reactive backflow loss P_{bf} under the control strategy I is calculated as

$$P_{bf}=\frac{L_m}{2(1-2D_1)f}\left[\frac{nV_{\mathrm{out}}d_D(1-d_D)}{L_{\mathrm{r}}}+\frac{V_{\mathrm{in}}D_1(2D_1-1)}{2L_m}\right]^2. \tag{31}$$

Similarly, the system circulating current I_m and reactive backflow loss under control strategies II, III, and IV are calculated, and the results are given in Table I.

By comparison, control strategy I has the less reactive backflow loss which is not affected by the phase shift d_F. When the circuit parameters are fixed, the reactive backflow loss P_{bf} can

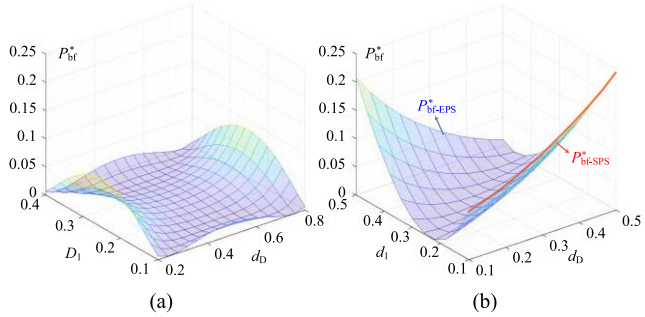

Fig. 9. Comparison of reactive backflow loss between HB-DAB converter and DAB converter. (a) Half-bridge cascaded DAB. (b) DAB under SPS, EPS control.

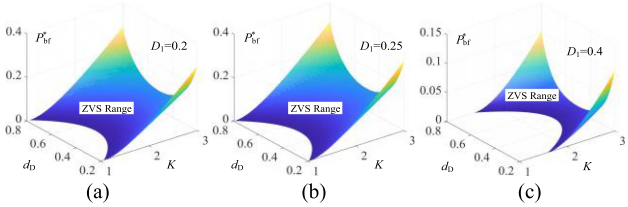

Fig. 10. Comparison of reactive backflow loss under different conditions. (a) $D_1 = 0.2$. (b) $D_1 = 0.25$. (c) $D_1 = 0.4$.

be regarded as a function of the phase shift d_D and the duty cycle D_1. According to the system output power formula (16), the proportion of reactive backflow loss in the process of energy transfer is calculated as follows:

$$P^*_{bf} = \left\{ \frac{D_1(1-2D_1)L_r V_{\text{in}} + 2d_D\left(d_D-1\right)L_m n V_{\text{out}}}{D_1(1-2D_1)L_r V_{\text{in}} - 2d_D\left(d_D-1\right)L_m n V_{\text{out}}} \right\}^2 \tag{32}$$

where $P^*{}_{bf} = P_{bf}/(P_{bf} + P_{\text{out}})$.

Fig. 9 shows the comparison of the standardized reactive backflow power $P^*{}_{bf}$ between HB-DAB converter and DAB converter, under the same voltage gain condition, with the variation of the phase shift d_D and the duty cycle D_1.

For the convenience of expression, d_1 represent the intra-bridge phase shift in the traditional DAB converter. As shown in Fig. 9(b), when the primary and secondary voltages of the DAB converter do not match, the reactive backflow loss is relatively large. With the increase of the phase shift d_D, the reactive backflow loss of the DAB converter shows an increasing trend. When the phase shift d_D is greater than 0.5, the reactive backflow loss increases rapidly.

By comparison, the HB-DAB converter has less reactive backflow loss, especially under the full load condition. On the other hand, the reactive backflow loss of the HB-DAB converter is symmetrically distributed with respect to the inter-bridge phase shift d_D, which expands the control range of the inter-bridge phase shift, and makes the control more flexible.

Fig. 10 shows the distribution of reactive backflow loss in the soft switching range of the HB-DAB converter under different voltage gain conditions. According to Fig. 10(a)–(c) and formula (31), the reactive backflow loss is symmetrical about the duty cycle $D_1 = 0.25$. With the increase of $|D_1\text{-}0.25|$, the reactive backflow loss of the system decreases, but the soft switching range of switch Q_1 decreases at the same time.

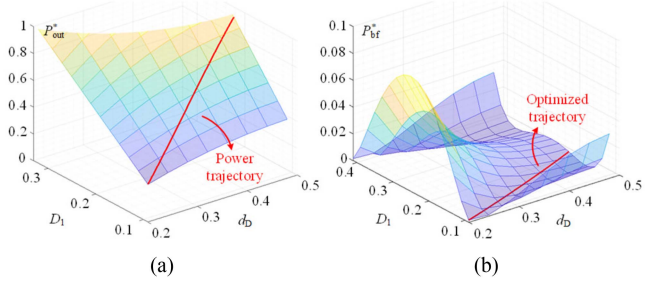

Fig. 11. Control trajectories for reactive backflow loss optimization. (a) Normalized output power. (b) Normalized reactive backflow.

The duty cycle D_1 and phase shift d_D affect both the output power P_{out} and the reactive backflow loss of the HB-DAB converter. Therefore, with duty ratio D_1 and phase shift d_D as the control degrees of freedom, the Karush–Kuhn–Tucker (KKT) function with reactive backflow loss as the optimization objective function is established. The power transfer function is used as the equality constraint, and the soft switching condition of the switch Q_1 is used as the inequality constraint

$$L\left(d_D, D_1, \lambda, \mu\right) = P_{bf} + \lambda\left(P_{\text{out}} - P_o\right) + \mu\left[i_{Lm}(t_1) - i_{\text{ZVS}}\right] \tag{33}$$

where i_{ZVS} represents the critical current of switch Q_1 to achieve soft switching. To simplify the analysis, when the current $i_{Lm}(t_1)$ is reversed, the switch Q_1 can realize ZVS.

Based on the KKT condition, the Lagrange function in formula (33) can be calculated as follows:

$$\begin{cases} \partial L/\partial d_{\text{D}} = 0 & \partial L/\partial D_1 = 0 \\ \partial L/\partial \lambda = 0 & \partial L/\partial \mu = 0 \end{cases}. \tag{34}$$

The decoupling relations between D_1 and d_D is

$$D_1 = \frac{1}{4}\left(1 - \left(\frac{L_r V_{\text{in}} - 16 L_m n V_{\text{out}} d_D(1-d_D)}{L_r V_{\text{in}}}\right)^{\frac{1}{2}}\right). \tag{35}$$

To simplify system control, the decoupling function (35) is approximated by interval linearization, and the linearized decoupling relationship is obtained as

$$D_1 = \frac{2L_m n V_{\text{out}} d_D}{L_r V_{\text{in}}} - \frac{L_m n V_{\text{out}}}{L_r V_{\text{in}}} + \frac{C_{pi}}{4}. \tag{36}$$

According to the above analysis, the optimized control trajectory of reactive backflow loss is drawn in Fig. 11. It can be seen that the output power of the system is stable, and the reactive backflow loss is obviously optimized.

IV. Experimental Verification

A. Parameter Design of the Converter

The inductor L_r is the core part of the energy transfer of the DAB circuit. To reduce the current stress of the current i_{Lr} and expand the adjustment range of the shift phase d_D, the inductor L_r should take a larger value under the condition of satisfying

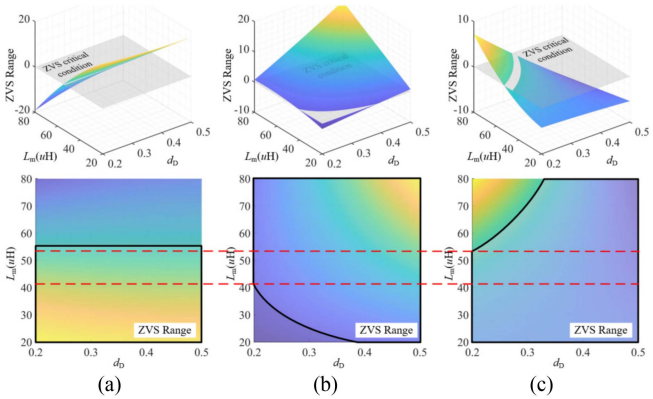

Fig. 12. Soft switching range of Q_1, S_1 and S_2 at 450 V input voltage. (a) Q_1 ZVS turn-ON. (b) S_1 ZVS turn-ON. (c) S_2 ZVS turn-ON.

the output power. According to the output power of the system, the inductor L_r is calculated as 6.8 uH.

The parameters of energy storage inductor L_m have great influence on the soft switching range of partial switches. According to the soft switching condition of switch Q_1 shown in formula (21), the soft-switching critical condition of switch Q_1 can be calculated as

$$L_m < \frac{D_1 K(1-2D_1)}{2d_D(1-d_D)} L_r. \tag{37}$$

Substitute the control trajectory of formula (36) into the above formula, and calculate the inductor L_m that satisfies Q_1 to realize ZVS turn-ON as follows:

$$L_m < \frac{K}{4(1-2d_D^2)} L_r. \tag{38}$$

Similarly, the inductance parameter of the shared switches to realize ZVS turn-ON are calculated as

$$\begin{cases} S_1 : L_m > \frac{2D_1K(2D_1+2d_F-1)}{1-2d_D-2D_1K-4d_D(1-d_D)} L_r \\ S_2 : L_m < \frac{2D_1K(2D_1+2d_F-1)}{2d_D-1+2D_1K-4d_D(1-d_D)} L_r \end{cases}. \tag{39}$$

Substitute the control trajectory of formula (36) into the formula (39), and calculate the inductor L_m that satisfies S_1 and S_2 to realize ZVS turn-ON. According to the above analysis, under the high voltage gain condition, the soft switching range of switches Q_1, S_1 and S_2 varied with inductor L_m are shown in Fig. 12. With the increase of inductor L_m, the soft switching range of switches Q_1 and S_2 decreases, while the soft switching range of switch S_1 increases. There is an inductance L_m parameter interval which can always realize Q_1, S_1 and S_2 ZVS turn-ON.

In addition, considering the influence of inductor L_m value on the effective value of the inductor current $i_{Lm}(t)$, the RMS value of current $i_{Lm}(t)$ is calculated as follows:

$$\begin{aligned} I_{Lm-\mathrm{RMS}}^2 = &[(B^2 - C^2 + AB + AC)d_F \\ &+ (C^2 + 4A^2 + AC) \\ &+ (2B^2 + 2BC + C^2 - A^2 - AC)D_1]/6 \end{aligned} \tag{40}$$

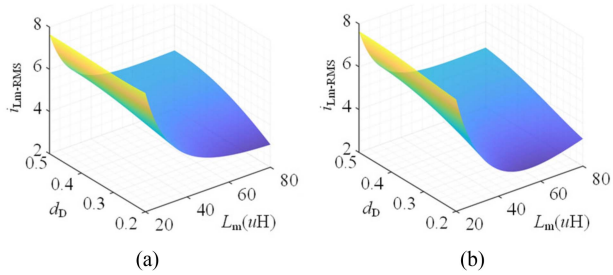

Fig. 13. Surface diagram of $i_{\mathrm{Lm\text{-}RMS}}$ varying with inductor L_m under different D_1 conditions. (a) Fixed duty cycle D_1. (b) Optimized duty cycle D_1.

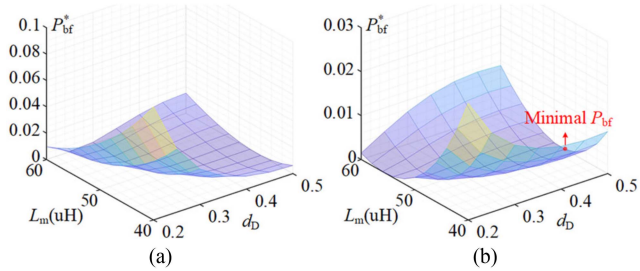

Fig. 14. Surface diagram of reactive loss varying with inductor L_m. (a) Fixed duty cycle D_1. (b) Optimized duty cycle D_1.

where the expressions for *A, B,* and *C* are as follows:

$$\begin{aligned} A &= i_{Lm}(t_0) = I_m, B = i_{Lm}(t_3) = I_m - \frac{d_F D_1 V_{\mathrm{in}}}{L_m f} \\ C &= i_{Lm}(t_9) = I_m - \frac{d_F D_1 V_{\mathrm{in}}}{L_m f} + \frac{D_1(1-2D_1)V_{\mathrm{in}}}{L_m f}. \end{aligned} \tag{41}$$

Fig. 13 shows the variation of the $i_{Lm}(t)$ RMS value with different inductance L_m values. Under the condition of fixed duty ratio D_1, the effective value of inductor current i_{Lm} decreases rapidly with the increase of inductor L_m, as shown in Fig. 13(a). However, the soft switching range of Q_1 is significantly reduced. When the duty cycle D_1 adopts optimal control, as the inductor L_m increases, the duty cycle D_1 gradually decreases to maintain the soft switching of the switch Q_1. When the inductor L_m is greater than 60 μH, duty cycle D_1 operates in the extreme duty cycle condition, the voltage across the inductor L_m is large, and the effective value of inductor current i_{Lm} increases.

According to formula (32), Fig. 14 shows the change of the reactive backflow loss with the phase shift d_D and inductor L_m under the condition of fixed shift phase D_1 and the condition of optimized duty cycle D_1. Under the condition of fixed D_1, with the increase of L_m, the freewheeling effect L_m is enhanced, and reactive backflow loss can be reduced. While, under the condition of low L_m, the reactive backflow loss accounts for a large proportion. On the contrary, according to Fig. 14(b), the reactive backflow loss no longer changes monotonically with L_m, which can be optimized in the whole operation range. This proves the effectiveness of the optimal control.

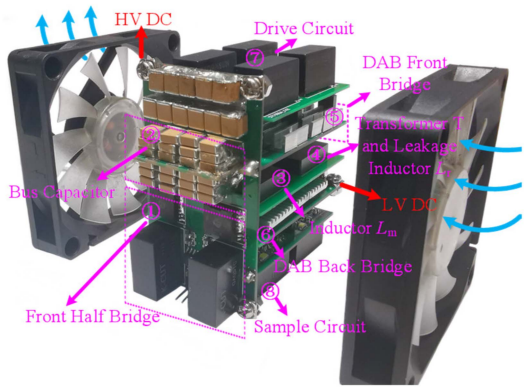

Fig. 15. Diagram of the experimental prototype.

TABLE II
PROTOTYPE SPECIFICATIONS

Specification/Parameter	Value
Input Voltage Range V_{in}	450–360 V
Rated Input Voltage V_{in}	400 V
Rated Output Voltage V_{out}	48 V
Rated power P_{out}	500 W
Switching Frequency f	100 kHz
Transformer Turns Ratio n	3
Energy Storage inductor L_m	42 uH
Leakage inductor L_r/n^2	6.8 uH
Energy storage capacitor C_b	150 uF
Switches	IMBG65R057M1H

B. Experimental Prototype Test

According to the above theoretical analysis, a prototype is constructed and tested to verify the circuit characteristics of the proposed converter. The experimental prototype is shown in Fig. 15. Table II gives the parameters of the experimental prototype. According to the optimized design of parameters, the inductor L_m is 42 uH, and the inductance L_r is 6.8 uH. To obtain high voltage gain at low turns ratio, the turns ratio N of the transformer is designed to be 3. To maintain the stability of the bus voltage $V_{\rm bus}$ and reduce the disturbance of the input voltage of the DAB circuit, the value of the bus capacitor C_b is selected as 150 uF.

Figs. 16 and 17, respectively, shows the soft switching situation of all the switches under full load condition and half-load condition, when the converter operates in the buck mode with a rated input voltage of 400 V. It can be seen that all the switches can realize ZVS turn-ON, under full load and half-load conditions. Fig. 18 shows the waveform of voltage V_{ab} and V_{cd} and the current waveform of inductance L_m and L_r. It can be seen that voltage V_{ab} and V_{cd} are stable and the system has stable output. Moreover, according to the current of the inductor L_m, the reactive backflow loss of the system is low, and the circulating current I_m is close to zero.

Experimental test waveforms of input voltage at 450 and 360 V are shown in Figs. 19–24. Corresponding, the output voltage and current waveform of backward boost mode are shown in Fig. 25. Within a wide input voltage range, the converter has good soft switching characteristics and low reactive backflow

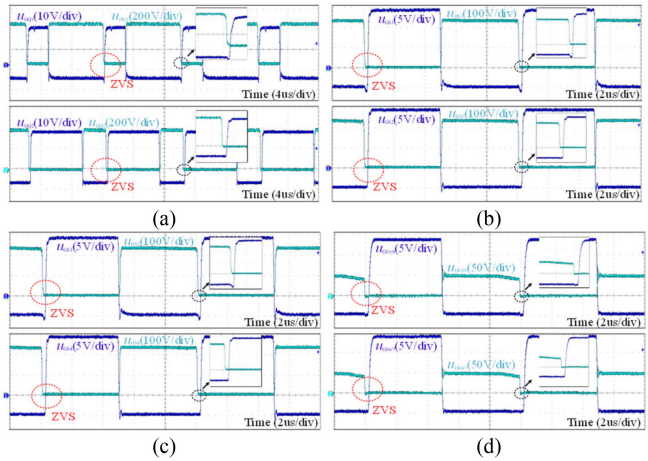

Fig. 16. ZVS-ON waveform of 400 V input voltage under full load condition. (a) Q_1 and Q_2. (b) S_1 and S_2. (c) S_3 and S_4. (d) S_5, S_6, S_7, and S_8.

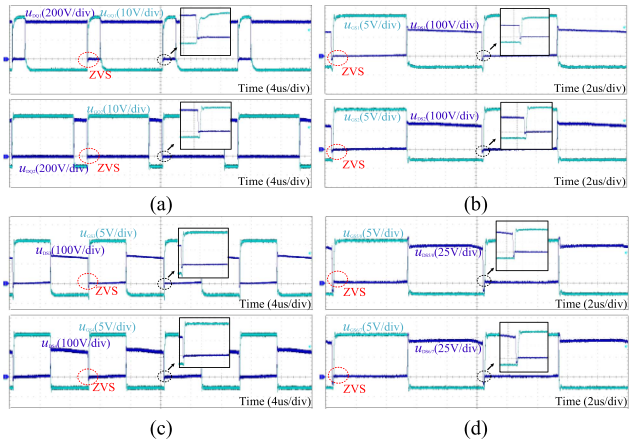

Fig. 17. ZVS-ON waveform of 400 V input voltage under half load condition. (a) Q_1 and Q_2. (b) S_1 and S_2. (c) S_3 and S_4. (d) S_5, S_6, S_7, and S_8.

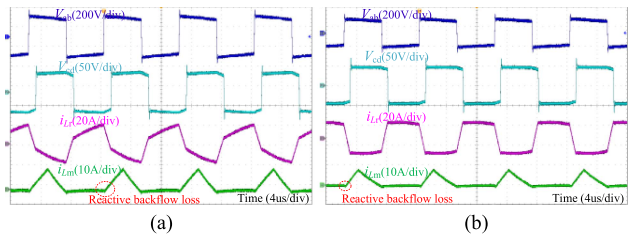

Fig. 18. Output voltage and current waveform of 400 V input voltage. (a) Output in full load condition. (b) Output in half load condition.

loss. The system can achieve high voltage gain and stable output under the condition of less turns ratio. The experimental results can prove the correctness and rationality of the theoretical analysis.

Fig. 26 shows the test efficiency comparison curves of the HB-DAB converter under different transmission power and input voltage conditions. By dismantling the half bridge HB_1, the test of traditional DAB converter is carried out. Under high voltage gain condition, serious mismatch of voltages causes large losses in DAB converters. Compared with the traditional

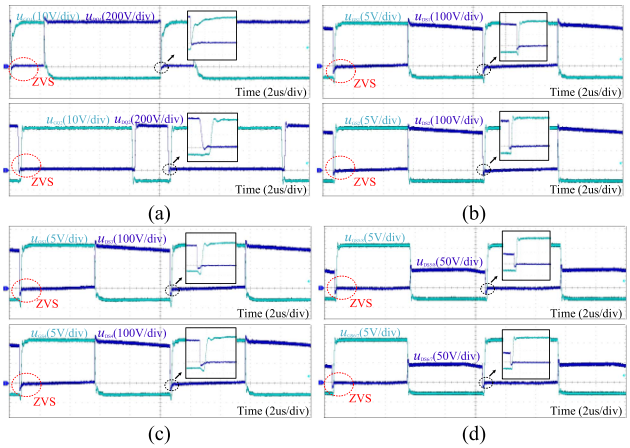

Fig. 19. ZVS-ON waveform of 450V input voltage under full load condition. (a) Q_1 and Q_2. (b) S_1 and S_2. (c) S_3 and S_4. (d) S_5, S_6, S_7, and S_8.

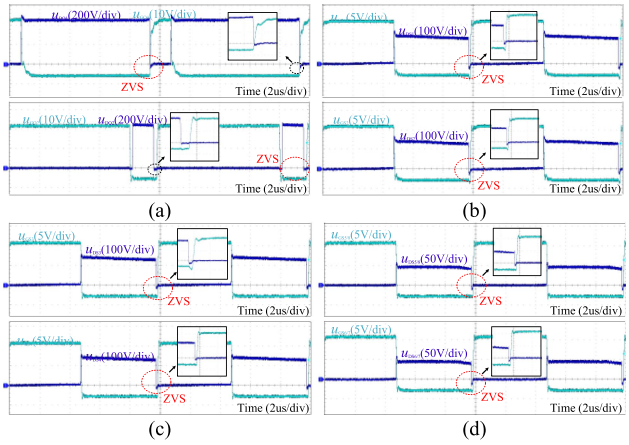

Fig. 20. ZVS-ON waveform of 450 V input voltage under half load condition. (a) Q_1 and Q_2. (b) S_1 and S_2. (c) S_3 and S_4. (d) S_5, S_6, S_7, and S_8.

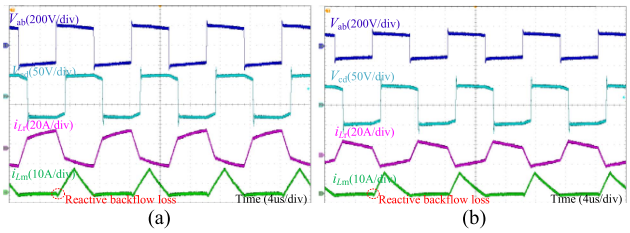

Fig. 21. Output voltage and current waveform of 450 V input voltage. (a) Output in full load condition. (b) Output in half load condition.

DAB converter, the proposed HB-DAB converter can maintain high efficiency and satisfy the design specifications with stable output. In addition, the maximum efficiency can reach about 94.2%.

A comparison between the HB-DAB converter and other optimized DAB converters is given in Table III. At present, in most references, DAB converter operates in the voltage matching state to improve the soft switching range of the system. However, under the condition of high voltage gain, more coil windings will lead to the increase of the core volume and window area of the transformer. This article considers to obtain high gain

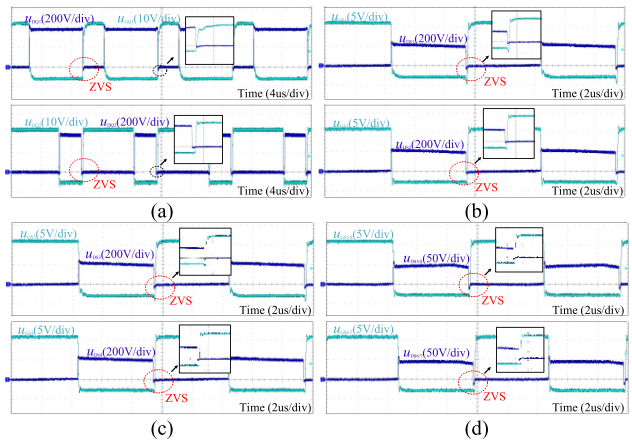

Fig. 22. ZVS-ON waveform of 350V input voltage under full load condition. (a) Q_1 and Q_2. (b) S_1 and S_2. (c) S_3 and S_4. (d) S_5, S_6, S_7, and S_8.

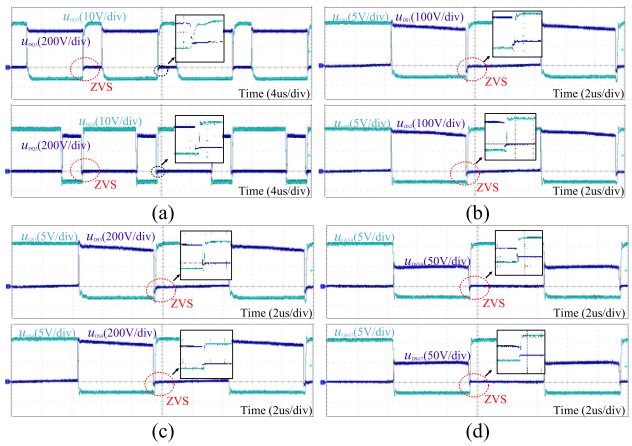

Fig. 23. ZVS-ON waveform of 350V input voltage under half load condition. (a) Q_1 and Q_2. (b) S_1 and S_2. (c) S_3 and S_4. (d) S_5, S_6, S_7, and S_8.

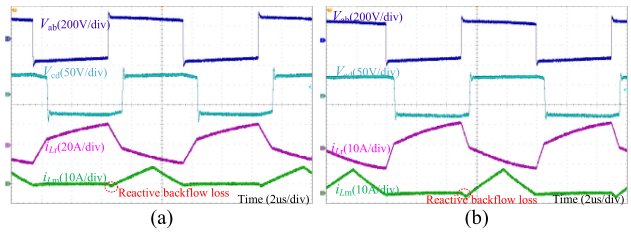

Fig. 24. Output voltage and current waveform of 350 V input voltage. (a) Output in full load condition. (b) Output in half load condition.

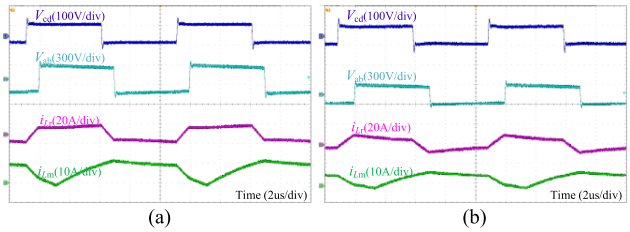

Fig. 25. Output voltage and current waveform of boost mode. (a) Output in full load condition. (b) Output in half load condition.

TABLE III
COMPARISON WITH OTHER OPTIMIZED DAB CONVERTERS

Article	Modulation	Objective of optimization	Input/ Output	Frequency	Turns ratio	Power level	Peak efficiency
[26]	EPS	ZVS	400 V/48 V	250 kHz	20:6	500W	95%
[29]	EPS	ZVS +Reactive	100 V/25 V	20 kHz	1:1	2kW	92.6%
[30]	EPS	ZVS +Reactive	114 V/100 V	20 kHz	1.1:1	545W	93.56%
[32]	AEPS+TPS	ZVS +RMS	400 V/48 V	50 kHz	6.6:1	5kW	97.7%
[36]	EPS	Reactive loss	140 V/70 V	20 kHz	2:1	200W	90.2%
[37]	APWM	RMS current	200 V/50 V	50 kHz	66:28	625W	95%
[38]	APWM	RMS current	380 V/56 V	50 kHz	76:15	500W	95.5%
HB-DAB	PWM+SPS	ZVS +Reactive	400 V/48 V	100 kHz	3:1	500W	94.2%

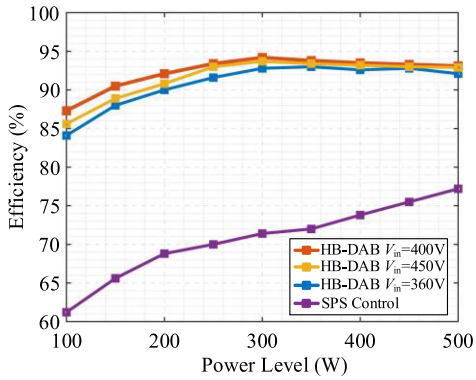

Fig. 26. Efficiency versus output power plot of the proposed converter.

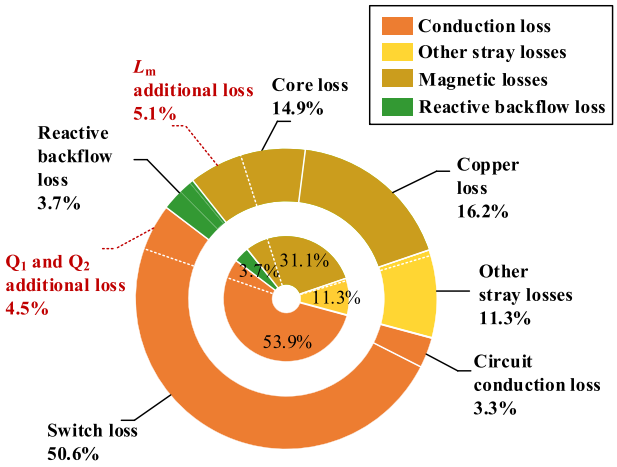

Fig. 27. Experimental prototype loss distribution.

at low turns ratio and achieving a wide soft-switching range. The HB-DAB converter expands the buck-boost capability of the system and has high efficiency in the bidirectional energy transmission process. The modular structure and simple control make the proposed converter show potential in the application of low voltage energy storage system.

Fig. 27 shows the loss distribution of the experimental prototype under the full load condition. The main part of the loss is the conduction loss of the switches on the output side. This is due to the inherent large RMS current under high voltage gain and the large ON-resistance of the switches. The efficiency of the system can be further improved by selecting switches with lower on-resistance and increasing the copper thickness of the circuit on the PCB board.

V. CONCLUSION

To optimize the performance of DAB converters in dc microgrids with high voltage gain, a HB-DAB converter based on partial switch sharing is designed in this article. Compared with the DAB converter, the proposed converter can achieve high voltage gain under less turn ratio. According to the KKT function, the converter realizes multiobjective optimal control. The system has good soft switching characteristics and low reactive backflow loss. It can realize the high efficiency of energy transmission and reduce the disturbance of the energy storage system to the dc microgrid. Moreover, the circuit parameters are optimized and a 500 W experimental prototype is tested. The experimental results can prove the correctness of the theoretical analysis, and the proposed converter shows good performance at high voltage gain condition.

REFERENCES

[1] G. Aiello, F. Gennaro, A. Imbruglia, and M. Cacciato, "High efficiency bidirectional sic-based power converter for V2G/V2H applications in a nano/microgrid scenario," in *Proc. AEIT Int. Conf. Elect. Electron. Technol. Automot.*, 2020, pp. 1–6.

[2] Y. Xuan, X. Yang, W. Chen, T. Liu, and X. Hao, "A novel NPC dual-active-bridge converter with blocking capacitor for energy storage system," *IEEE Trans. Power Electron.*, vol. 34, no. 11, pp. 10635–10649, Nov. 2019.

[3] K. C. Tseng, S. Y. Chang, and C. A. Cheng, "Novel isolated bidirectional interleaved converter for renewable energy applications," *IEEE Trans. Ind. Electron.*, vol. 66, no. 12, pp. 9278–9287, Dec. 2019.

[4] N. Kondrath, "Bidirectional DC-DC converter topologies and control strategies for interfacing energy storage systems in microgrids: An overview," in *Proc. IEEE Int. Conf. Smart Energy Grid Eng.*, 2017, pp. 341–345.

[5] A. Joseph and P. Balachandra, "Smart grid to energy internet: A systematic review of transitioning electricity systems," *IEEE Access*, vol. 8, pp. 215787–215805, 2020.

[6] Y. F. Wang, L. K. Xue, C. S. Wang, P. Wang, and W. Li, "Interleaved high-conversion-ratio bidirectional DC–DC converter for distributed energy-storage systems: Circuit generation, analysis, and design," *IEEE Trans. Power Electron.*, vol. 31, no. 8, pp. 5547–5561, Aug. 2016.

[7] K. Tytelmaier, O. Husev, O. Veligorskyi, and R. Yershov, "A review of non-isolated bidirectional dc-dc converters for energy storage systems," in *Proc. II Int. Young Scientists Forum Appl. Phys. Eng.*, 2016, pp. 22–28.

[8] Q. Xu, N. Vafamand, L. Chen, T. Dragičević, L. Xie, and F. Blaabjerg, "Review on advanced control technologies for bidirectional DC/DC converters in DC microgrids," *IEEE J. Emerg. Sel. Topics Power Electron.*, vol. 9, no. 2, pp. 1205–1221, Apr. 2021.
[9] R. Li and F. Shi, "Control and optimization of residential photovoltaic power generation system with high efficiency isolated bidirectional DC–DC converter," *IEEE Access*, vol. 7, pp. 116107–116122, 2019.
[10] X. Pan, H. Li, Y. Liu, T. Zhao, C. Ju, and A. K. Rathore, "An overview and comprehensive comparative evaluation of current-fed-isolated-bidirectional DC/DC converter," *IEEE Trans. Power Electron.*, vol. 35, no. 3, pp. 2737–2763, Mar. 2020.
[11] B. Zhao, Q. Song, and W. Liu, "Power characterization of isolated bidirectional dual-active-bridge DC–DC converter with dual-phase-shift control," *IEEE Trans. Power Electron.*, vol. 27, no. 9, pp. 4172–4176, Sep. 2012.
[12] B. Zhao, Q. Song, W. Liu, and Y. Sun, "Overview of dual-active-bridge isolated bidirectional DC–DC converter for high-frequency-link power-conversion system," *IEEE Trans. Power Electron.*, vol. 29, no. 8, pp. 4091–4106, Aug. 2014.
[13] W. Shi, J. He, J. Song, and S. Yang, "Unified-Phase-Shift control method of dual active bridge DC-DC converter for data center application," in *Proc. IEEE Sustain. Power Energy Conf.*, 2021, pp. 3199–3203.
[14] C. Wang, G. Sha, H. Cheng, and Q. Deng, "Unified phasor analytical method for dual-active-bridge DC/DC converter under phase-shift control," in *Proc. IEEE 8th Int. Power Electron. Motion Control Conf.*, 2016, pp. 348–355.
[15] B. Zhao, Q. Song, J. Li, W. Liu, G. Liu, and Y. Zhao, "High-frequency-link DC transformer based on switched capacitor for medium-voltage DC power distribution application," *IEEE Trans. Power Electron.*, vol. 31, no. 7, pp. 4766–4777, Jul. 2016.
[16] D. Aggeler, J. Biela, and J. W. Kolar, "A compact, high voltage 25 kW, 50 kHz DC-DC converter based on SIC JFETs," in *Proc. 23rd Annu. IEEE Appl. Power Electron. Conf. Expo.*, 2008, pp. 801–807.
[17] H. Li et al., "Influences of device and circuit mismatches on paralleling silicon carbide MOSFETs," *IEEE Trans. Power Electron.*, vol. 31, no. 1, pp. 621–634, Jan. 2016.
[18] B. Zhao, Q. Song, J. Li, Y. Wang, and W. Liu, "Modular multilevel high-frequency-link DC transformer based on dual active phase-shift principle for medium-voltage DC power distribution application," *IEEE Trans. Power Electron.*, vol. 32, no. 3, pp. 1779–1791, Mar. 2017.
[19] M. Liserre, M. Andresen, L. Costa, and G. Buticchi, "Power routing in modular smart transformers: Active thermal control through uneven loading of cells," *IEEE Ind. Electron. Mag.*, vol. 10, no. 3, pp. 43–53, Sep. 2016.
[20] N. M. L. Tan, T. Abe, and H. Akagi, "Design and performance of a bidirectional isolated DC–DC converter for a battery energy storage system," *IEEE Trans. Power Electron.*, vol. 27, no. 3, pp. 1237–1248, Mar. 2012.
[21] F. Wu, S. Fan, X. Li, and S. Luo, "Bidirectional buck-boost current-fed isolated DC-DC converter and its modulation," *IEEE Trans. Power Electron.*, vol. 35, no. 5, pp. 5506–5516, May 2020.
[22] Z. Zhang, K. Tomas-Manez, Y. Xiao, and M. A. E. Andersen, "High voltage gain dual active bridge converter with an extended operation range for renewable energy systems," in *Proc. IEEE Appl. Power Electron. Conf. Expo.*, 2018, pp. 1865–1870.
[23] Y. F. Wang, B. Chen, Y. Hou, Z. Meng, and Y. Yang, "Analysis and design of a 1-MHz bidirectional multi-CLLC resonant DC–DC converter with GaN devices," *IEEE Trans. Ind. Electron.*, vol. 67, no. 2, pp. 1425–1434, Feb. 2020.
[24] Y. Xiao, Z. Zhang, M. A. E. Andersen, and K. Sun, "Impact on ZVS operation by splitting inductance to both sides of transformer for 1-MHz GaN based DAB converter," *IEEE Trans. Power Electron.*, vol. 35, no. 11, pp. 11988–12002, Nov. 2020.
[25] W. Chen, P. Rong, and Z. Lu, "Snubberless bidirectional DC–DC converter with new CLLC resonant tank featuring minimized switching loss," *IEEE Trans. Ind. Electron.*, vol. 57, no. 9, pp. 3075–3086, Sep. 2010.
[26] G. Xu, L. Li, X. Chen, Y. Liu, Y. Sun, and M. Su, "Optimized EPS control to achieve full load range ZVS with seamless transition for dual active bridge converters," *IEEE Trans. Ind. Electron.*, vol. 68, no. 9, pp. 8379–8390, Sep. 2021, doi: 10.1109/TIE.2020.3014562.
[27] X. Liu et al., "Novel dual-phase-shift control with bidirectional inner phase shifts for a dual-active-bridge converter having low surge current and stable power control," *IEEE Trans. Power Electron.*, vol. 32, no. 5, pp. 4095–4106, May 2017, doi: 10.1109/TPEL.2016.2593939.
[28] K. Wu, C. W. de Silva, and W. G. Dunford, "Stability analysis of isolated bidirectional dual active full-bridge DC–DC converter with triple phase-shift control," *IEEE Trans. Power Electron.*, vol. 27, no. 4, pp. 2007–2017, Apr. 2012, doi: 10.1109/TPEL.2011.2167243.
[29] J. Tian, F. Wang, F. Zhuo, Y. Wang, H. Wang, and Y. Li, "A zero-backflow-power EPS control scheme with multi-objective coupled-relationship optimization in DAB-based converter," *IEEE J. Emerg. Sel. Topics Power Electron.*, vol. 10, no. 4, pp. 4128–4145, Aug. 2022.
[30] F. Xu, J. Liu, and Z. Dong, "Minimum backflow power and ZVS design for dual-active-bridge DC–DC converters," *IEEE Trans. Ind. Electron.*, vol. 70, no. 1, pp. 474–484, Jan. 2023.
[31] A. Tong, L. Hang, G. Li, X. Jiang, and S. Gao, "Modeling and analysis of a dual-active-bridge-isolated bidirectional DC/DC converter to minimize RMS current with whole operating range," *IEEE Trans. Power Electron.*, vol. 33, no. 6, pp. 5302–5316, Jun. 2018.
[32] M. Mahdavifard, N. Mazloum, F. Zahin, A. KhakparvarYazdi, A. Abasian, and S. A. Khajehoddin, "An asymmetrical DAB converter modulation and control systems to extend the ZVS range and improve efficiency," *IEEE Trans. Power Electron.*, vol. 37, no. 10, pp. 12774–12792, Oct. 2022.
[33] H. Shi, H. Wen, Y. Hu, and L. Jiang, "Reactive power minimization in bidirectional DC–DC converters using a unified-phasor-based particle swarm optimization," *IEEE Trans. Power Electron.*, vol. 33, no. 12, pp. 10990–11006, Dec. 2018.
[34] Y. Tang et al., "Artificial intelligence-aided minimum reactive power control for the DAB converter based on harmonic analysis method," *IEEE Trans. Power Electron.*, vol. 36, no. 9, pp. 9704–9710, Sep. 2021.
[35] Q. Liu, Q. Qian, B. Ren, S. Xu, W. Sun, and L. Yang, "A two-stage buck–boost integrated LLC converter with extended ZVS range and reduced conduction loss for high-frequency and high-efficiency applications," *IEEE J. Emerg. Sel. Topics Power Electron.*, vol. 9, no. 1, pp. 727–743, Feb. 2021.
[36] H. Shi et al., "Minimum-backflow-power scheme of DAB-based solid-state transformer with extended-phase-shift control," *IEEE Trans. Ind. Appl.*, vol. 54, no. 4, pp. 3483–3496, Jul./Aug. 2018.
[37] S. Chakraborty and S. Chattopadhyay, "Fully ZVS, minimum RMS current operation of the dual-active half-bridge converter using closed-loop three-degree-of-freedom control," *IEEE Trans. Power Electron.*, vol. 33, no. 12, pp. 10188–10199, Dec. 2018.
[38] E. L. Carvalho, C. A. Felipe, L. V. Bellinaso, C. M. d. O. Stein, R. Cardoso, and L. Michels, "Asymmetrical-PWM DAB converter with extended ZVS/ZCS range and reduced circulating current for ESS applications," *IEEE Trans. Power Electron.*, vol. 36, no. 11, pp. 12990–13001, Nov. 2021.

Yiliang Li was born in Heilongjiang Province, China, in 1996. He received the B.S. and M.S. degrees in electrical engineering in 2018 and 2020, respectively, from Harbin Institute of Technology, (HIT), Harbin, China, where he is currently working toward the Ph.D. degree in electrical engineering with the School of Electrical Engineering and Automation.

His current research interests include bidirectional dc–dc converter, electric vehicle charging and energy storage system.

Yijie Wang (Senior Member, IEEE) was born in Heilongjiang Province, China, in 1982. He received the B.S., M.S. and Ph.D. degrees in electrical engineering from Harbin Institute of Technology, (HIT), Harbin, China, in 2005, 2007 and 2012, respectively.

From 2012 to 2014, he was a Lecturer with the Department of Electrical and Electronics Engineering, Harbin Institute of Technology. From 2014 to 2017, he was an Associate Professor with the Department of Electrical and Electronics Engineering, Harbin Institute of Technology. Since 2017, he has been a Professor with the Department of Electrical and Electronics Engineering, Harbin Institute of Technology. His interests include dc–dc converters, soft-switching power converters, power factor correction circuits, digital control electronic ballasts, LED lighting systems.

Dr. Wang is an Associate Editor for IEEE TRANSACTIONS ON INDUSTRIAL ELECTRONICS, IEEE JOURNAL OF EMERGING AND SELECTED TOPICS IN POWER ELECTRONICS, IEEE ACCESS, *IET Power Electronics and Journal of Power Electronics.*

Yueshi Guan (Senior Member, IEEE) was born in Heilongjiang Province, China, in 1990. He received the B.S., M.S. and Ph.D. degrees in electrical engineering from Harbin Institute of Technology (HIT), Harbin, China, in 2013, 2015 and 2019, respectively.

Since 2019, he has been an Associate Professor with the Department of Electrical and Electronics Engineering, HIT. His research interests include of high frequency and very high frequency converters, single-stage ac/dc converter, and high conversion ratio converters.

Dianguo Xu (Fellow, IEEE) was born in Heilongjiang, China, in 1960. He received the B.S. degree in control engineering from Harbin Engineering University, Harbin, China, in 1982, and the M.S. and Ph.D. degrees in electrical engineering from Harbin Institute of Technology (HIT), Harbin, China, in 1984 and 1989, respectively.

In 1984, he was an Assistant Professor with the Department of Electrical Engineering, HIT. Since 1994, he has been a Professor with the Department of Electrical Engineering, HIT. He was the Dean of School of Electrical Engineering and Automation, HIT, from 2000 to 2010. He is now the vice president of HIT. He has authored or coauthored more than 600 technical papers. His research interests include renewable energy generation technology, power quality mitigation, sensor less vector-controlled motor drives, high performance servo system.

Dr. Xu is an Associate Editor for IEEE TRANSACTIONS ON INDUSTRIAL ELECTRONICS and IEEE Journal of Emerging and Selected Topics in Power Electronics. He is currently the Chairman of IEEE Harbin Section.